Microstructural topology optimization for patch-based sandwich panel with desired in-plane thermal expansion and structural stiffness

Zihao Yang[a], Yongcun Zhang[a,*], Shutian Liu[a], Zhangming Wu[b]

[a] State Key Laboratory of Structural Analysis for Industrial Equipment, Dalian University of Technology, Dalian, 116024, China

[b] Cardiff School of Engineering, Queens Buildings, The Parade, Newport Road, Cardiff CF24 3AA, UK

Corresponding author: yczhang@dlut.edu.cn

Abstract: Apart from the lightweight and excellent mechanical properties, sandwich panels can be endowed with tailorable in-plane coefficient of thermal expansion (CTE) through an elaborate design of periodic face-sheets. However, albeit that the microstructural topology of their periodic face-sheets promises unique thermal expansion behaviors, it may also bring significant influences to the structural stiffness of sandwich panels. In this study, we apply the topology optimization method to design face-sheet microstructures to enable the sandwich panels to possess desired in-plane CTEs, lightweight and benign mechanical properties, simultaneously. By introducing the patch-based cell as initial configuration, the existing thermally-bending adjustment mechanism for thermal deformation control is integrated to the process of topology optimization. The entire topology optimization process including the equivalent mechanical properties prediction and the sensitivity computation is performed within an in-house programme coupled with commercial finite element analysis software. To this end, a matching numerical sensitivity analysis method to extract sensitivities straightforwardly from software's output is also developed on the basis of asymptotic homogenization method. Three types of specific optimization problems in terms of different objective functions and constraint conditions are proposed, solved and studied, namely, in-plane zero thermal expansion combining with maximum stiffness, the other for in-plane zero thermal expansion optimal specific stiffness, and minimizing in-plane isotropic thermal expansion. Some specific resulting topologies, microstructural features and design details are subsequently obtained. In particular, the current strategy of integrating effective mechanism and topological technology can be extended to design more microstructures for simultaneously tailorable CTE and high mechanical performance by replacing present thermal deformation control mechanism with others.

Keywords: Topology optimization; Thermal expansion; Microstructural design; Sandwich panel; Sensitivity analysis

1. Introduction

Most natural bulk materials exhibit the feature of positive thermal expansions. Fortunately, artificial materials, particular of the recent developed metamaterials (Ni et al. 2019; Xu et al. 2017; Zhu et al. 2018) with well-designed constituents and void space, could break the conventional boundary and create possibility for achieving tailorable coefficient of thermal expansion (CTE) ranging from large positive to negative including zero CTE. Owing to the superior functionality of controllable thermal expansion, these metamaterials have great potentials of wide applications in civil engineering (Takenaka and Koshi 2012), aerospace structures (Steeves and Evans 2011; Wei et al. 2018), precision instruments (Steeves and Evans 2011b; Zhengchun et al. 2016) and hypersonic vehicles (Chen et al. 2006; Yamamoto et al. 2014) where often experience large variations of temperature and are sensitive to thermal distortion. With the development of advanced manufacturing processes, especially additive manufacturing methods, it provides a tremendous opportunity to fabricate new materials with sophisticated topological structures and distinct properties, however, due to increasingly harsh material service environment and multi-functional demands, remains ongoing challenge to discover and innovate novel materials with unprecedented mechanical properties to meet the demands of target engineering applications.

Up to present, the most metamaterials with tailorable CTEs are devised from experience and intuition. The mechanism for the effective control of thermal deformation that was developed is subsequently introduced into the purposeful design of basic cell-microstructures. The existing tailorable CTE metamaterials, according to different thermal deformation mechanism, can be divided into three categories, namely, bending-dominated (Lakes 2007), stretching-dominated (Steeves et al. 2007) and Poisson contraction (Lehman and Lakes 2013). These pioneering research works only arrived a few preliminary design remarks, therefore much more valuable design concepts and methods must be provided to further develop tailorable CTE metamaterials. Shortly afterwards, a number of metamaterials with tailorable CTEs are subsequently developed by Wei et al. (2016, 2018), Xu et al. (2017b, 2016), Zhang et al. (2018,2019) and others (Wu et al. 2016; Xie et al. 2018a,2018b). Note, the intuitive-based design approach through tuning the mechanism to obtain unique material properties is natural and effective, but after all, the design results are largely rely on the intuition and experience from the designers. Consequently, very limited design options can be utilized for developing new and advanced microstructure forms after exhausting of new ideas in designing structural forms.

As an alternative, the topology optimization method offers a systematic, non-intuitive, and mathematically-driven strategy to design novel materials and structures (Ai and Gao 2019; Andreassen et al. 2014; Zhang et al. 2018). Through optimizing the distribution of constituents and void space within a spatial domain, the desired material characteristics could be achieved automatically. In this pertinent field, Sigmund and Torquato (1999,1997) was the pioneer who firstly applied the so-called three-phases topology optimization method to design periodic microstructures with extreme thermal expansion attribute combining stiffness limitation. Compared with the design results given by the intuitive-based method, the topological microstructures usually feature of complicated geometry. Nevertheless, the developed imaginative topological structures not only enrich the design types of tailorable CTE metamaterials but also inspire the designers on devising intuitive-based materials which implied topological principle. Some recent research works have approved this, such as Xie et al. (2017) proposed an annulus with zero thermal expansion coefficient (ZTE), in which the fork-like lattice cell design inspired more or less from a topology designed annulus structure with high radial stiffness and low CTE (Wang et al. 2011). Note, although few research studies (Takezawa et al. 2015; Wang et al. 2011; Watts and Tortorelli 2017) in early times had been explored the advantages of applying topology optimization methods in designing novel tailorable CTE materials, they are unable to arrive any new mechanisms for the thermal deformation control. As a result, due to the limited applications of topological technology, very few published research works that developed the topological microstructures compared with that applying of intuitive-based design methods can be found in the open literatures.

Until recently a new design concept of dual-constituent sandwich panels with bidirectional in-plane ZTE originally proposed by the present authors (Zhang et al. 2019). Such kind of design has great application potential in acreage thermal protection systems from providing the possibility of avoiding the thermal stress failure and undesired thermal deformation of exterior surfaces for hypersonic vehicle (Steeves et al. 2007). In the past designs, the inevitable gaps included in the outer face sheet are the chief drawback because the exterior aerodynamic heat enters into interior structure easily. This disadvantage is successfully avoided through the newly designed sandwich panel, where the outer face sheets are all solid and not porous. The counterintuitive properties of in-plane ultralow thermal expansion are attributed from the special design of upper and lower face sheets, both of which are attached with an additional layer of patch with high CTE to cause in-plane contraction deformation. In further study we carried out parametric study (Yang et al. 2019) to investigate the optimal stiffness design with combining in-plane zero thermal expansion. Several key design aspects including the patch covering form and shape are confirmed as important aspects that bring obvious influences on effective structural stiffness and control effectiveness of in-plane thermal expansion. Therefore, it is reasonable to expect that further designing the microstructural topologies of patch will generate optimal cells that will simultaneously possess desired CTEs and mechanical performances.

Thus in this paper, we attempt to combine the existing mechanism of thermal deformation control and the topology optimization method together to develop an integrated method for designing microstructures with desired CTEs, lightweight and mechanical properties, simultaneously. This research idea is achieved through introducing the originally designed microstructure for the face-sheets cells of the patch-based sandwich panels mentioned above. The remainder of this paper is organized as follows: in Section 2, we review the original design of patch-based lattice sandwich panels and the involving thermally bending-adjustment mechanism for in-plane thermal deformation controlling are clarified; Section 3 presents the three types of specific optimization problems in terms of mathematical formulations; The NIAH method adopted for predicting effective cell properties is introduced in Section 4 and the theoretical derivations of newly proposed numerical sensitivity analysis method is also given. Section 5 completes several typical design examples using present unified strategy and topology optimization procedure. Conclusions are drawn in Section 6.

2. Original design of patch-based sandwich panel with tailorable in-plane CTEs

Fig.1 shows the original design of patch-based lattice sandwich panel of which the tailorable in-plane CTE is attributed to the well-designed periodic face sheets. In this design, the center area of each basic cell is a bi-layer structural form that possesses equal bi-directional initial curvatures along both of the two orthogonal directions. The tunability of thermally induced in-plane expansion is originated from central bi-layer parts that made of two perfectly bonded layers of differing CTE achieved through attaching an additional layer of patch with high CTE to the substrate.

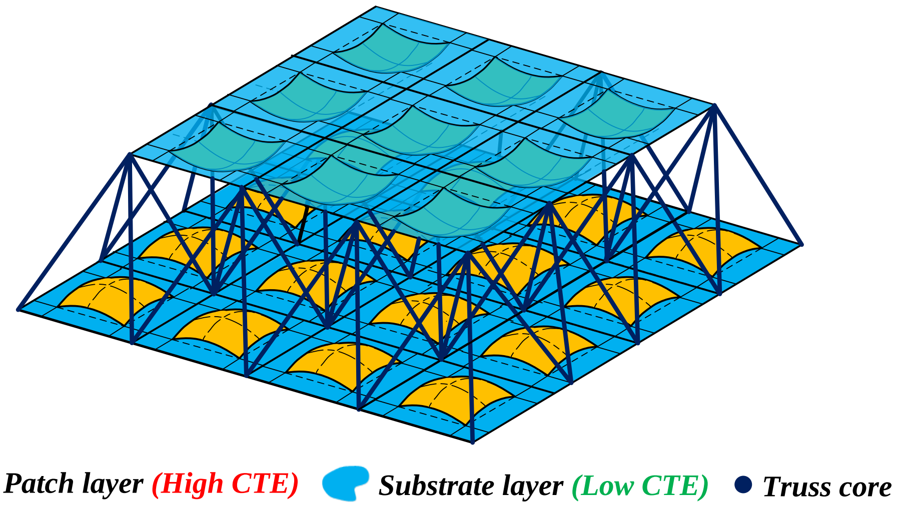

Fig.1. The whole configuration of original patch-based lattice sandwich panel with tailorable in-plane CTEs.

Fig.2II illustrates the process of cell in-plane dimensional adjustment caused by ambient temperature variation, solely. The mechanism introduced to control in-plane thermal deformation, named the thermally bending-adjustment mechanism, utilizes the thermal expansion mismatch within bi-layer parts to trigger transverse bending to the cell during temperature variation, which subsequently results in the in-plane contraction that can compensate simultaneously produced in-plane thermal expansion of single-layer parts. The truss core provides the necessary support for the face-sheets by connecting four corner points of every periodic cell. In doing so, the same transverse bending deformation is ensured in each local cell to prevent the possible overall transverse deformation of upper and lower face-sheets during the thermal loading. Note that the truss core has little effect on effective in-plane CTEs of face-sheet due to the huge difference of in-plane stiffness between the lattice core and face sheets. Consequently, by designing the values of face-sheet cell geometric parameters including side length ratio q of center area length L_0 to cell length L , the curved angle θ and the thicknesses of substrate layer t_1 and patch layer t_2, the tailorable in-plane CTEs range from positive to negative (not only confining to zero) values are achieved.

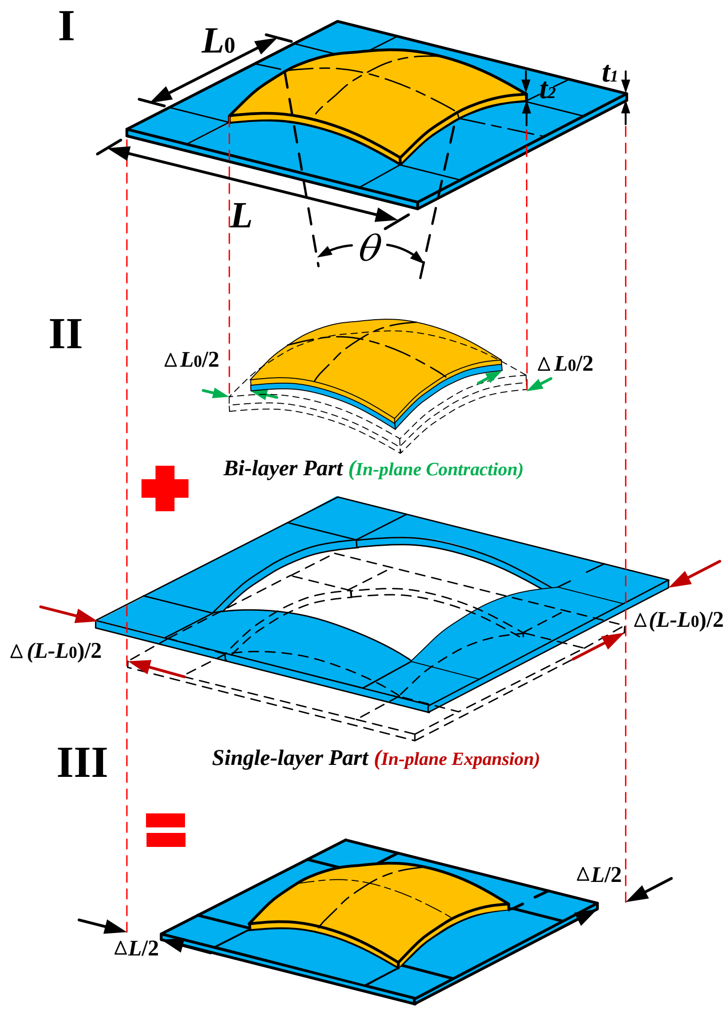

Fig.2. The process of cell in-plane dimensional adjustment caused by ambient temperature variation, solely. (I) Configuration of basic cell with geometric parameter definitions. (II) Deformations of bi-layer, single-layer parts and their corresponding dimensional changes ΔL_0 and $\Delta(L-L_0)$, respectively. (III) Actual deformation of cell along with in-plane dimensional change ΔL due to thermally induced transverse bending.

One of the key designs to control in-plane thermal expansion is that the bi-layer part of face sheets should be included with sufficient initial curvature, which can enlarge the magnitude of thermally induced transverse bending to compensate simultaneously produced in-plane thermal expansion. Adopting excessive small curvature may lead to cell insufficient in-plane contractions, and as a consequence, it inevitably fails in tuning cell in-plane thermal expansion. However, it is apparent that the in-plane stiffness of face sheets reduce significantly due to bending deformation as a result of the designed cell's slight curvature. In the meantime a further parametric study (Yang et al. 2019) indicated that, when desired in-plane CTE is achieved, the in-plane stiffness of the cell and thermal deformation control effectiveness are closely related to the material distribution within the patch layer. This mechanism has been proved through comparing the results of original cell configuration shown in Fig.3(a) with those of other design schemes with partial covered patches shown in Fig.3(b)-(c). Therefore, it is reasonable to speculate that a further design of microstructural topologies for the patch layer, such as a hypothetical topological shape shown in Fig.3(d), will lead to an optimal design of cells, which will possess desired CTEs (range from negative to positive), lightweight and benign mechanical performance with a sufficient load carrying capacity of sandwich structures.

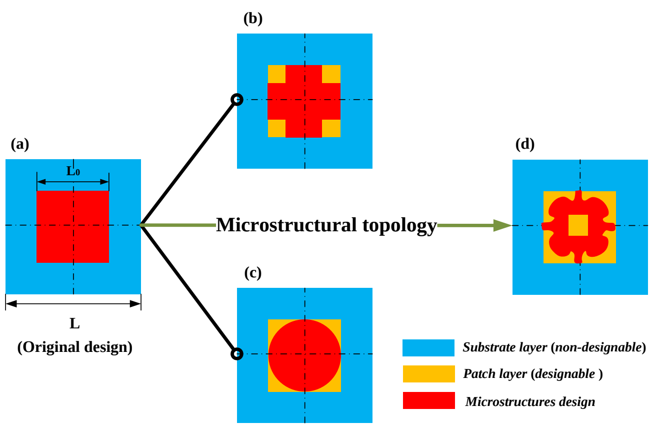

Fig.3. The sketches of (a) : the original design of the face-sheet cell. (b)-(c):comparison schemes of the face-sheet cell with partially covered patches (Yang et al. 2019). (d):a hypothetical topological result used for the purpose of illustration.

3. Optimization problem description and formulation

In this work, based on the original design of cell configuration as shown in Fig.3(a), we adopt the method of structural topology optimization to tailor the material distribution in yellow patch layer, which is located at the square area in the center of the face-sheet cell. The blue non-designable layer is configured with lower CTE and bidirectional initial curvatures, which follow the original design scheme developed in refer (Yang et al. 2019). The designable layer possessing higher CTE is partially covered on the non-designable layer, which enables the designable layer to be a non-planar surface due to the presence of initial curvatures. However, the optimization process herein is still appropriate to be considered as a plane problem because the effective properties including CTEs and stiffness coefficients are all in-plane properties, and the optimization does not considered the thickness variation. Additionally, for practical applications, only isotropic thermal expansion of each cell along two in-plane orthogonal directions is considered during the process of topology optimization.

The optimization problem in terms of objective functions, design variables and constrain conditions including above features presented as follows:

Design variables and material interpolation schemes: The square designable layer within each cell is firstly discretized into *N* finite elements. With such pattern of finite element, the design problem becomes assigning high CTE material or void for each element and minimizing the objective function with respect to element material density. In order to obtain the designed cells with isotropic in-plane thermal expansion, a 8-order symmetry pattern over the square domain is imposed for the design of material distribution of designable layer. Therefore, only on 1/8 yellow region of the entire designable layer as illustrated in Fig.4 needs to be optimized for designing the distribution of material, which also leads to significant reduction of computational cost for the optimization process.

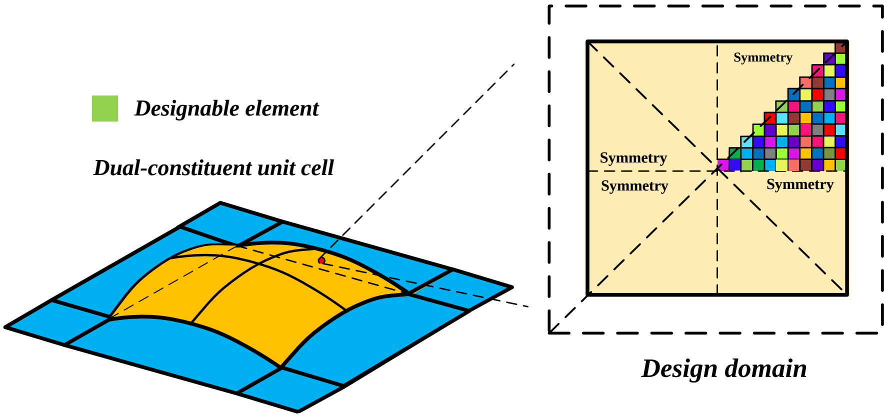

Fig.4. The 1/8 designable layer and discretization for the present topology optimization problem considering in-plane thermal isotropy. Each square represents one finite element which can consist of high CTE material or void.

A density design variable $\rho_e \in [\rho_{\min}, 1]$ is then defined for each element, with which "void" is represented as $\rho_e = \rho_{\min}$ (non-zero in order to avoid singularity of stiffness matrix) and solid material is given by $\rho_e = 1$. Using SIMP approach to define the interpolation between material density and material mechanical properties, the local Young's modulus in each element e can be written as a function of the design variable ρ_e as,

$$E_e(\rho_e) = \rho_e^{\eta} E_{high} \tag{1}$$

where E_{high} is the Young's modulus of material with high CTE; η is a penalization factor introduced to drive the density distribution towards the so-called black-and-white solution. Note, the local thermal expansion coefficient α_e does not depend on the design variable ρ_e due to the fact that thermal expansion coefficient does not change with density.

Objective functions: Three different objective functions corresponding to three typical optimization problems with respect to practical engineering applications are defined. The first two design objectives are both defined for achieving in-plane ZTE. Meanwhile, apart from designing with desired in-plane CTEs, the sandwich structures are required to be stiff and lightweight for integrated function combing sufficient load-carrying capacity. Due to that the primary loading for sandwich constructions, both in-plane and bending, are carried by the faces. Thus, the structural mechanical performances ought to be further considered by (1) maximizing the in-plane stiffness of face-sheet cell without material volume constraint; (2) maximizing specific stiffness combining in-plane stiffness and face-sheet cell weight.

In the first optimization case, an effective bulk modulus in terms of in-plane stiffness coefficients is defined as $k^*=(\mathrm{E}_{11}+\mathrm{E}_{22}+2\mathrm{E}_{12})/4$, which is adopted as an index to represent the mechanical performance of designing cells. The objective function is then expressed as,

$$-k_{ss}=-\frac{k^*}{k} \tag{2}$$

where k is a constant representing the bulk modulus of flat substrate layer. The ratio $k_{ss}=k^*/k$ we introduced herein is to quantitate the inevitable in-plane stiffness loss given rise by the initial curvature, which is for obtaining desired functionality of tailorable in-plane thermal expansion. The minus sign is used to convert the maximization problem into a minimization problem.

On the other hand, the previous study (Yang et al. 2019) indicated that the designs for ZTE with high stiffness usually lead to the increase weight of cells. Hence, in the second optimization case, we proposed a more comprehensive optimization problem that is considering the in-plane stiffness and face-sheet cell weight, simultaneously. By introducing a factor of material volume fraction f_V as the weight index to normalize the in-plane stiffness loss ratio, the second objective function is defined as,

$$-k_{sp}=-\frac{k_{ss}}{f_V}=-\frac{k^*/k}{\frac{1}{V}\sum_{e=1}^{N}\rho_e V_e} \tag{3}$$

where V_e and V are the material volumes of an element e and the flat substrate layer, respectively; f_V is the ratio of total volume of microstructural topologies in the patch layer to that of the flat substrate layer. The expression given in Eq.(3) can be regarded as the generalized specific stiffness if replace the traditional density term with weight index. The second objective function will lead to the resulting optimal designs to possess high-stiffness and lightweight, simultaneously.

In fact, apart from the feature of near-zero thermal expansion, the negative CTEs can also be achieved through designing material distribution in the patch layer. Therefore, in the third optimization case, we minimizing the in-plane thermal expansion towards to negative values. The sum of effective CTEs α^* along the horizontal and vertical directions is adopted as the objective function of this optimization case and given as follows,

$$\alpha^*_{min} = \alpha^*_1 + \alpha^*_2 \tag{4}$$

where subscripts *1* and *2* represent the horizontal and vertical directions, respectively. Note, the optimization problem defined by Eq.(4) will also approve an interesting surmise that the in-plane minimized thermal expansion can be realized by the optimal distribution of finite volume high CTE material within the patch layer, whereas excessive high CTE material could not bring further decrease on effective CTEs.

Constraint conditions: The design of in-plane ZTE needs be implemented as the constraint condition in the first two optimization problems. However, it is inappropriate to directly impose the absolute zero value of effective CTE ($\alpha^*=0$) as the constraint condition into the optimization formulation. Thus, instead of directly setting $\alpha^*=0$, we apply the following ratio α_i^* / α_1 as the constraint condition,

$$(\alpha_i^* / \alpha_1)^2 \le 1\times 10^{-4} \quad i = 1, 2 \tag{5}$$

where α_1 is the CTE of constituent material with lower thermal expansion. Eq.(5) defines the effective CTE that is bound between $-0.01\alpha_1 \le \alpha^* \le 0.01\alpha_1$, i.e., at least two orders magnitude decrease on CTE compared with that of constituent material.

The final optimization formulations: The optimization formulations according to different optimization problems are summarized as in the followings,

Optimization problem 1,

$$\begin{aligned} &\text{Find: } \boldsymbol{\rho_e};\\ &\text{Minimize: } -k_{ss}(\rho_e);\\ &\text{Subject to: } (\alpha_1^*/\alpha_1)^2 \le 1\times e^{-4},\ (\alpha_2^*/\alpha_1)^2 \le 1\times e^{-4}\\ &\qquad 0 \le \rho_{\min} \le \rho_e \le 1 \ \ (e=1,2,\ldots,N). \end{aligned} \tag{6}$$

Optimization problem 2,

$$\begin{aligned} &\text{Find: } \boldsymbol{\rho_e};\\ &\text{Minimize: } -k_{sp}(\rho_e);\\ &\text{Subject to: } (\alpha_1^*/\alpha_1)^2 \le 1\times e^{-4},\ (\alpha_2^*/\alpha_1)^2 \le 1\times e^{-4}\\ &\qquad 0 \le \rho_{\min} \le \rho_e \le 1 \ \ (e=1,2,\ldots,N). \end{aligned} \tag{7}$$

Optimization problem 3,

$$\begin{aligned} &\text{Find: } \boldsymbol{\rho_e};\\ &\text{Minimize: } \alpha^*_{min}(\rho_e); \end{aligned}$$

Subject to: $0 \le \rho_{\min} \le \rho_e \le 1$ ($e=1,2,\ldots,N$) . (8)

where $\boldsymbol{\rho_e} = \{\rho_1, \rho_2, \ldots \rho_N\}^T$ is the N-vectors of density design variables and ρ_{min} is the corresponding lower limit be given value of 1×10^{-4} for all of the optimization case studies in this work. Note, that 8-order symmetry pattern we imposed for the square cell patch is only sufficient to ensure the isotropic in-plane thermal expansion properties, but does not also imply the mechanical isotropy.

4. NIAH-based effective property prediction and sensitivity analysis

The asymptotic homogenization (AH) method was previously developed to determine the effective properties of periodic composites. Based on this method, optimization were carried out by many researchers to find structures with extreme or prescribed effective properties (Sigmund 1995; Bendsoe and Kikuchi 1988), which is called inverse homogenization method. In the AH method, the macroscopic displacement field is expressed using a small-parameter perturbation,

$$u_{\zeta}(\boldsymbol{x},\boldsymbol{y}) = u_0(\boldsymbol{x},\boldsymbol{y}) + \zeta^1 u_1(\boldsymbol{x},\boldsymbol{y}) + \zeta^2 u_2(\boldsymbol{x},\boldsymbol{y}) + O(\zeta^3) \tag{9}$$

where $\boldsymbol{x}$ and $\boldsymbol{y}$ are the vectors of the macroscopic and microscopic coordinates. Here ξ (0< ξ <1) is a small parameter denoting characteristic dimension of the unit cell. With introduction of fast variable $\boldsymbol{y}$, field variable $\boldsymbol{u}$ will vary macroscopically with slow variable $\boldsymbol{x}$, and at the same time, vary rapidly in microscopic scale with fast variable $\boldsymbol{y}$.

Considering only the first-order terms in the asymptotic expansion in (9), the effective elastic modulus of the unit cell can be written in the energy form as,

$$\boldsymbol{E}_{ij}^{H} = \frac{1}{|Y|}\int_Y (\boldsymbol{\varepsilon}^{0(i)} - \boldsymbol{\varepsilon}^{*(i)})^T \boldsymbol{D} (\boldsymbol{\varepsilon}^{0(j)} - \boldsymbol{\varepsilon}^{*(j)}) dY \tag{10}$$

where Y is the cell domain and $|Y|$ is the unit cell volume; $\boldsymbol{D}$ is the constitutive stiffness matrix of material. Note, the effective elastic modulus expressed by Eq.(10) can be determined numerically through a novel implementation algorithm of asymptotic homogenization (NIAH) proposed by Cheng et al. (2013a). The NIAH has the merit that the algorithm can be executed easily using commercial finite element analysis (FEA) software as a black box. In this study, within the framework of NIAH, we develop a complete set of topology optimization procedure to design the periodic microstructures with desired CTE and high stiffness, simultaneously. The new optimization procedure includes two main parts, one is the prediction of effective properties including elastic modulus and CTEs, and the other is a newly developed matching numerical sensitivity analysis method.

Firstly, applying the NIAH to predict the effective CTE (NIAH-CTE) (Zhang et al. 2017) and elastic modulus of periodic microstructures is introduced. The prediction process can be executed using any commercial FEA software by applying specific nodal force fields and thermal loads to the cell finite element model, the effective elastic modulus $\boldsymbol{E}^{\boldsymbol{H}}$ and thermos-elastic constant $\boldsymbol{\beta}^{\boldsymbol{H}}$ can be extracted directly from the software output of static analyses. The effective CTE $\boldsymbol{\alpha}^{\boldsymbol{H}}$ is then determined using the equation as follows,

$$\boldsymbol{\alpha}^{\boldsymbol{H}} = (\boldsymbol{E}^{\boldsymbol{H}})^{-1}\boldsymbol{\beta}^{\boldsymbol{H}} \tag{11}$$

As an open-source numerical prediction method, the detailed implementation and execution steps of NIAH-CTE can be found in (Zhang et al. 2017). Note, the prediction process for the effective properties of periodic microstructures in our optimization problems is implemented as a (2D) plane problem, which has been explained at the beginning of Section 3. As a result, the initial nodal displacement fields $\boldsymbol{\chi}^{\boldsymbol{0(i)}}$ we firstly applied to the cell finite element model are selected as follows (Zhang et al. 2017),

$$\boldsymbol{\chi}^{\mathbf{0(i)}} = \begin{Bmatrix} u \\ v \end{Bmatrix}, \quad \boldsymbol{\chi}^{\mathbf{0(1)}} = \begin{Bmatrix} x \\ 0 \end{Bmatrix} \quad \boldsymbol{\chi}^{\mathbf{0(2)}} = \begin{Bmatrix} 0 \\ y \end{Bmatrix} \quad \boldsymbol{\chi}^{\mathbf{0(3)}} = \begin{Bmatrix} 0.5y \\ 0.5x \end{Bmatrix} \tag{12}$$

in which (u, v) are the displacements along x and y coordinate directions.

For a gradient-based optimization process, the sensitivity computation is indispensable for obtaining a topological solution. In order to cooperate NIAH-CTE that needed to be executed within FEA software, we proposed a matching numerical sensitivity analysis method (NSAM-CTE) to compute the sensitivity information for the effective CTE of periodic microstructures with respect to density design variable. With the NSAM-CTE, the sensitivity information of effective CTE in the form of element strain energy can be computed straightforwardly from the commercial FEA software, thus the tedious programming works for computing sensitivities are avoided. The theoretical derivation process for NSAM-CTE are presented as follows.

Considering the Eq.(11), the sensitivity of the effective CTE with respect to the density design variable ρ_e is expressed as,

$$\frac{\partial \boldsymbol{\alpha}_i^{\boldsymbol{H}}}{\partial \rho_e} = \frac{\partial (\boldsymbol{E}^{\boldsymbol{H}})^{-1}}{\partial \rho_e}\boldsymbol{\beta}^{\boldsymbol{H}} + (\boldsymbol{E}^{\boldsymbol{H}})^{-1}\frac{\partial \boldsymbol{\beta}^{\boldsymbol{H}}}{\partial \rho_e} \tag{13}$$

Because it is hard to directly compute the sensitivity information from the inversion form of the effective elastic modulus $\partial(\boldsymbol{E}^{\boldsymbol{H}})^{-1}/\partial\rho_e$, we apply the following mathematical conversion with the use of unit matrix $\boldsymbol{I}$ to overcome this issue,

$$(\boldsymbol{E}^{\boldsymbol{H}})^{-1} = (\boldsymbol{E}^{\boldsymbol{H}})^{-1}\boldsymbol{I} = (\boldsymbol{E}^{\boldsymbol{H}})^{-1}\boldsymbol{E}^{\boldsymbol{H}}(\boldsymbol{E}^{\boldsymbol{H}})^{-1} \tag{14}$$

With Eq.(14), the sensitivity of the inversion of the effective elastic modulus $\partial(\boldsymbol{E}^{\boldsymbol{H}})^{-1}/\partial\rho_e$ can be expressed by the sensitivity of the effective elastic modulus as,

$$\frac{\partial(\boldsymbol{E}^{\boldsymbol{H}})^{-1}}{\partial\rho_e} = -(\boldsymbol{E}^{\boldsymbol{H}})^{-1}\frac{\partial\boldsymbol{E}^{\boldsymbol{H}}}{\partial\rho_e}\boldsymbol{E}^{\boldsymbol{H}} \tag{15}$$

Substituting the Eq.(15) into Eq.(13), the completed expression of the sensitivity of the effective CTE without $\partial(\boldsymbol{E}^{\boldsymbol{H}})^{-1}/\partial\rho_e$ term is derived and expressed as,

$$\frac{\partial\boldsymbol{\alpha}_i^{\boldsymbol{H}}}{\partial\rho_e} = -(\boldsymbol{E}^{\boldsymbol{H}})^{-1}\frac{\partial\boldsymbol{E}^{\boldsymbol{H}}}{\partial\rho_e}\boldsymbol{E}^{\boldsymbol{H}}\boldsymbol{\beta}^{\boldsymbol{H}} + (\boldsymbol{E}^{\boldsymbol{H}})^{-1}\frac{\partial\boldsymbol{\beta}^{\boldsymbol{H}}}{\partial\rho_e} \tag{16}$$

The Eq.(16) indicates that the sensitivities of the effective CTEs largely depend on the sensitivities of the effective elastic modulus $\partial\boldsymbol{E}^{\boldsymbol{H}}/\partial\rho_e$ and thermos-elastic constant $\partial\boldsymbol{\beta}^{\boldsymbol{H}}/\partial\rho_e$. The later can be solved through a new numerical solution method with the expression of $\boldsymbol{\beta}^{\boldsymbol{H}}$ in the following energy form (Sigmund and Torquato 1997),

$$\boldsymbol{\beta}_i^{\boldsymbol{H}} = \frac{1}{|Y|}\int_Y (\boldsymbol{\varepsilon}^{\boldsymbol{0(i)}} - \boldsymbol{\varepsilon}^{*\boldsymbol{(i)}})^T \boldsymbol{D}(\boldsymbol{\alpha} - \boldsymbol{\varepsilon}^{\boldsymbol{\zeta}})dY \tag{17}$$

where $\boldsymbol{\varepsilon}^{\boldsymbol{0(i)}}$, $\boldsymbol{\varepsilon}^{*\boldsymbol{(i)}}$ and $\boldsymbol{\varepsilon}^{\boldsymbol{\zeta}}$ are the unit, characteristic and thermal strain fields defined in NIAH-CTE, respectively; $\boldsymbol{D}$ and $\boldsymbol{\alpha}$ are the constitutive stiffness and thermal expansion coefficient matrices of material. According to Eq.(17), the sensitivity of the effective thermos-elastic constant $\boldsymbol{\beta}^{\boldsymbol{H}}$ with respect to the density design variable ρ_e is derived analytically and expressed as,

$$\frac{\partial\boldsymbol{\beta}_i^{\boldsymbol{H}}}{\partial\rho_e} = \frac{1}{|Y|}\int_Y (\boldsymbol{\varepsilon}^{\boldsymbol{0(i)}} - \boldsymbol{\varepsilon}^{*\boldsymbol{(i)}})^T \frac{\partial\boldsymbol{D}}{\partial\rho_e}(\boldsymbol{\alpha} - \boldsymbol{\varepsilon}^{\boldsymbol{\zeta}})dY_e + \frac{1}{|Y|}\int_Y (\boldsymbol{\varepsilon}^{\boldsymbol{0(i)}} - \boldsymbol{\varepsilon}^{*\boldsymbol{(i)}})^T \boldsymbol{D}\frac{\partial\boldsymbol{\alpha}}{\partial\rho_e}dY_e \tag{18}$$

With the consideration of present material interpolation scheme given by Eq.(1), the last term in Eq.(18) is set to zero. Since the i-th design variable ρ_i is defined in the i-th element, the sensitivity formulation can be transformed from cell domain Y to the element domain Y_e,

$$\frac{\partial\boldsymbol{\beta}_i^{\boldsymbol{H}}}{\partial\rho_e} = \frac{1}{|Y|}\int_{Y_e} (\boldsymbol{\varepsilon}^{\boldsymbol{0(i)}} - \boldsymbol{\varepsilon}^{*\boldsymbol{(i)}})^T \frac{\partial\boldsymbol{D}_e(E_e)}{\partial\rho_e}(\boldsymbol{\alpha} - \boldsymbol{\varepsilon}^{\boldsymbol{\zeta}})dY_e \tag{19}$$

where $\boldsymbol{D}_e$ is the constitutive stiffness matrix of the element e. As the SIMP approach for material interpolation is applied, the sensitivity formulation can be further derived as,

$$\frac{\partial\boldsymbol{\beta}_i^{\boldsymbol{H}}}{\partial\rho_e} = \frac{2\eta}{\rho_e|Y|}\int_{Y_e}\frac{1}{2}(\boldsymbol{\varepsilon}^{\boldsymbol{0(i)}} - \boldsymbol{\varepsilon}^{*\boldsymbol{(i)}})^T \boldsymbol{D}_e(\boldsymbol{\alpha} - \boldsymbol{\varepsilon}^{\boldsymbol{\zeta}})dY_e \tag{20}$$

It should be noted that the expression in the integral sign is the mutual strain energy (defined as WB_e^i) of the element e corresponding to the generalized strain fields $(\boldsymbol{\varepsilon}^{\boldsymbol{0(i)}} - \boldsymbol{\varepsilon}^{*\boldsymbol{(i)}})$ and $(\boldsymbol{\alpha} - \boldsymbol{\varepsilon}^{\boldsymbol{\zeta}})$. The WB_e^i can be extracted from the output of FEA software after using a simple solution technique by defining a new generalized strain fields $\overline{\boldsymbol{\varepsilon}}^{\boldsymbol{i+\alpha}}$ as the sum of the strain fields $(\boldsymbol{\varepsilon}^{\boldsymbol{0(i)}} - \boldsymbol{\varepsilon}^{*\boldsymbol{(i)}})$ and $(\boldsymbol{\alpha} - \boldsymbol{\varepsilon}^{\boldsymbol{\zeta}})$,

$$\overline{\boldsymbol{\varepsilon}}^{i+\alpha} = (\boldsymbol{\varepsilon}^{0(i)} - \boldsymbol{\varepsilon}^{*(i)}) + (\boldsymbol{\alpha} - \boldsymbol{\varepsilon}^{\zeta}) \tag{21}$$

The corresponding element strain energy of the $\overline{\boldsymbol{\varepsilon}}^{i+\alpha}$ can be expressed as,

$$\begin{aligned} WB_e^{i+\alpha} &= \int_{Y_e} \frac{1}{2} (\overline{\boldsymbol{\varepsilon}}^{i+\alpha})^T \boldsymbol{D}_e (\overline{\boldsymbol{\varepsilon}}^{i+\alpha}) dY_e = \int_{Y_e} \frac{1}{2} (\boldsymbol{\varepsilon}^{0(i)} - \boldsymbol{\varepsilon}^{*(i)})^T \boldsymbol{D}_e (\boldsymbol{\varepsilon}^{0(i)} - \boldsymbol{\varepsilon}^{*(i)}) dY_e \\ &+ \int_{Y_e} \frac{1}{2} (\boldsymbol{\alpha} - \boldsymbol{\varepsilon}^{\zeta})^T \boldsymbol{D}_e (\boldsymbol{\alpha} - \boldsymbol{\varepsilon}^{\zeta}) dY_e + \int_{Y_e} (\boldsymbol{\varepsilon}^{0(i)} - \boldsymbol{\varepsilon}^{*(i)})^T \boldsymbol{D}_e (\boldsymbol{\alpha} - \boldsymbol{\varepsilon}^{\zeta}) dY_e \end{aligned} \tag{22}$$

Note that the first two terms in Eq.(22) are the element strain energies W_e^{ii} and WB_e^{α} corresponding to the generalized strain fields $\boldsymbol{\varepsilon}^{0(i)} - \boldsymbol{\varepsilon}^{*(i)}$ and $(\boldsymbol{\alpha} - \boldsymbol{\varepsilon}^{\zeta})$, respectively. Then, the mutual strain energy WB_e^{i} used for determining the sensitivity of the effective thermos-elastic constant in Eq.(20) is calculated by,

$$WB_e^{i} = (WB_e^{i+\alpha} - W_e^{ii} - WB_e^{\alpha}) / 2 \tag{23}$$

Consequently, the completed element sensitivity information of $\partial \boldsymbol{\beta}^{\boldsymbol{H}} / \partial \rho_e$ can be obtained through extracting element strain energies $WB_e^{i+\alpha}$, W_e^{ii} and WB_e^{α} from cell finite element model under corresponding generalized strain fields. It should be mentioned that the sensitivities of the effective elastic modulus $\partial \boldsymbol{E}^{\boldsymbol{H}} / \partial \rho_e$ can also be obtained using a similar method developed by Yi et al. (2016).

As one type of numerical sensitivity analysis method will be executed within FEA software, the implementation steps are convenient for users to understanding. Thus, we provide a full instruction for presenting the implementation steps of NSAM-CTE in Appendix A. Moreover, the effectiveness of the proposed NSAM-CTE is also verified with a simple verification example by comparing the sensitivity results with those of finite difference method (FDM). The comparing results show very well consistency with those given by FDM as presented in Appendix B.

On the basis of proposed topology optimization procedure, the whole process that integrates NIAH-CTE and NSAM-CTE for designing desired microstructures in Eqs. (6) - (8) is depicted in a flowchart as shown in Fig.5.

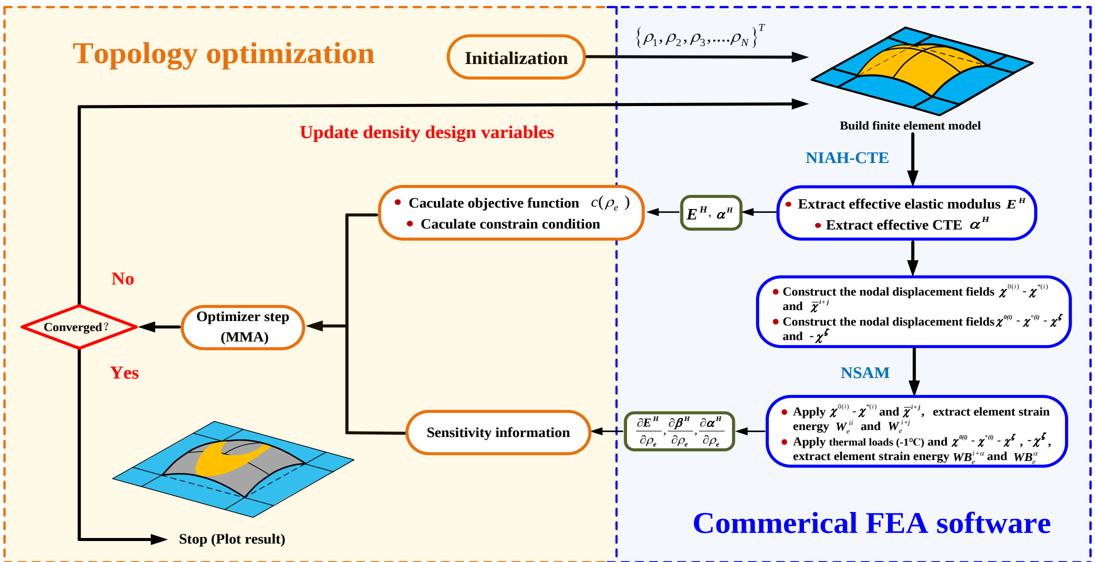

Fig.5. Flowchart of the design algorithm.

Firstly, after selecting specific objective function and constraint conditions, the initial density design variable leads to construct an initial finite element model of cell in FEA software (ANSYS 15.0 is adopted here). As shown in Fig.6, the material densities of all the elements along thickness direction are assumed to be equal with each other, i.e. mapping into one density design variable. As such, the topology optimization is effectively degraded to a plane problem, and the number of density design variables is significantly reduced;

Next, NIAH-CTE is applied and executed in FEA software to predict the effective in-plane CTEs and elastic modulus of present cell finite element model;

Subsequently, NSAM-CTE is adopted to solve the sensitivity of effective CTEs and using a similar method (Yi et al. 2016), the sensitivity of effective elastic modulus are also obtained. Note, due to the 8-order symmetry pattern and the above discussed one design variable mapping, the sensitivity for one certain design variable is not merely corresponding to one solid element. On the other hand, in the process of sensitivity calculation, the sensitivities belong to different solid elements but all related to the same specific design variable should be accumulated together. With NSAM-CTE, the computation of element strain energy replaces sensitivity analysis will be accumulated as the final sensitivity result;

Finally, all the sensitivity information and effective properties will pass into the MMA optimizer (The method of moving asymptotes) (Svanberg 1987) to calculate the values of objective function and constraint conditions, and subsequently update the density design variable. This iterative design procedure is repeated until the change in each density design variable is convergent to a set point. In addition, we implement the density filter to ensure the existence of feasible solutions for this topology optimization problem and avoid the formation of checkerboard patterns. A detailed discussions on this filter is given in (Bruns and Tortorelli 2001), and a corresponding benchmark example programmed by MATLAB can be found in another reference (Xia and Breitkopf 2015).

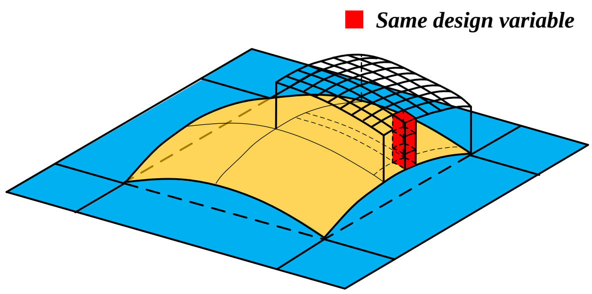

Fig.6. Illustration of design variable mapping.

5. Design examples

In this section, using the proposed topology optimization procedure, several typical design examples are carried out to find desired microstructures corresponding to the specific optimization targets defined in Eqs.(6)-(8). The designable layer with high CTE is subsequently discretized using 10800 eight-nod solid elements SOLID185 (in ANSYS 15.0), resulting in 60×60×3 elements. At least six solid elements solid elements, three for designable layer and another three for non-designable layer, are set along thickness direction in order to simulate the transverse bending deformation of cells during the process of temperature variation. The geometric features of the dual-constituent cell are defined using previous design parameters given in reference (Yang et al. 2019) , which are presented at the beginning of Section 2. The present geometric parameter L is taken as a unit length and side-to-thickness ratio L/ t_1 is 100 for equal thicknesses t_1 and t_2. Note, the optimization for the initial curvature and the area of design domain are not considered, thus, the curved angle θ and the side length ratio q are assumed to be constant values during the topology optimization process.

For materials selection, theoretically, it is allowed to use any arbitrary two types of materials with different positive CTEs for the constituent materials. In this work, alloy Invar is taken as low CTE material for the non-designable layer and Aluminum alloy is taken as high CTE material for the designable layer. The material properties of Invar and Aluminum alloy are listed in Table.1.

Table.1. The material properties (Lehman and Lakes 2013) of Invar and Aluminum alloy used in the process of topology optimization.

Material member	Young's Modulus E (GPa)	CTE α (ppm/°C)	Poisson's ratio v
Invar	140	1.0	0.28
Al 7075-T6	70	22.2	0.33

5.1 In-plane ZTE combining maximized stiffness

Regarding to the optimization problem defined by Eq.(2), the obtained optimal microstructures for in-plane ZTE and maximum stiffness are introduced, firstly. The topology optimization starts with the original design configuration given in Fig.3(a) as the initial design, and takes curved angle θ and side length ratio q as input design parameters for the comparison. The penalty factor and filter radius in present design examples are chosen as 3.0 and 1.5, respectively.

The optimization results for the design of cell microstructures are shown in Table.2 and corresponding 3D view of the entire cell shapes and 3×3 arrays are also displayed. The red and blue colors represent the materials with high and low CTE, respectively. The yellow border is the plane projection of designable layer which shows specific optimization design area. It has been seen that the optimization results have clear and smooth boundaries. The absolute values of objective function k_{ss} and high CTE material volume fraction f_v are listed below each group of the resulting designs.

Table.2. Optimization solutions of cell microstructure and corresponding 3D view of the entire cell shapes and

3×3 arrays of the optimized cells under different curved angle θ and side length ratio q. Note that the thicknesses of both high and low CTE layers in 3D view is magnified by 1.5 times for demonstration purpose.

$\theta\,(°)$	$q = 0.6$		$q = 0.7$	
	Unit cell	Array (3×3)	Unit cell	Array (3×3)
9.0	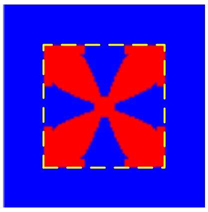	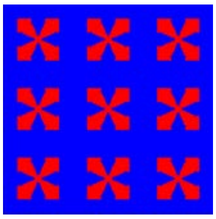	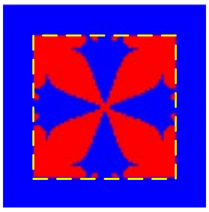	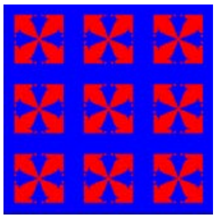
	(a) k_{ss} =0.472, f_V =0.230		(b) k_{ss} =0.389, f_V =0.315	
3D view	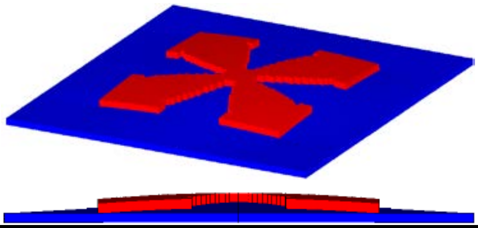		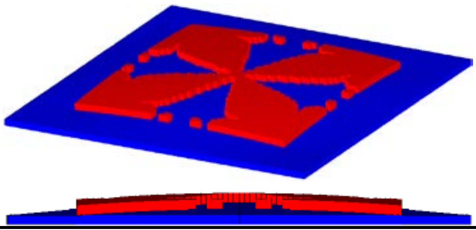	
6.0	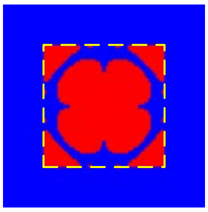	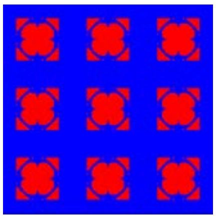	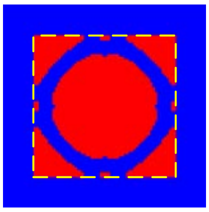	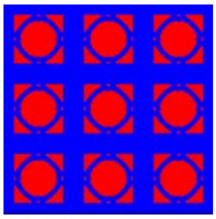
	(c) k_{ss} =0.598, f_V =0.256		(d) k_{ss} =0.517, f_V =0.338	
3D view	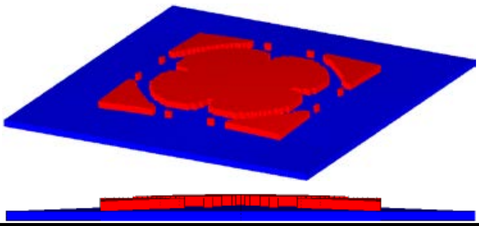		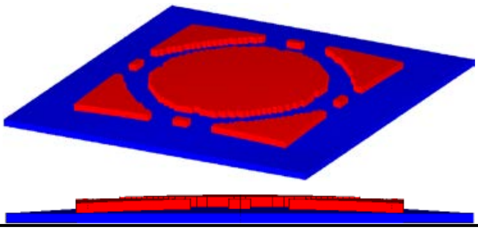	
4.5		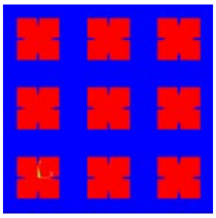	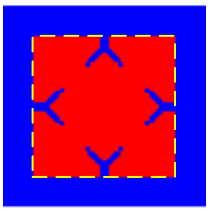	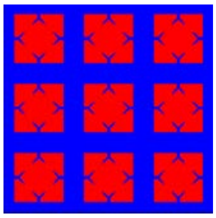
	(e) k_{ss} =0.703, f_V =0.346		(f) k_{ss} =0.629, f_V =0.452	
3D view	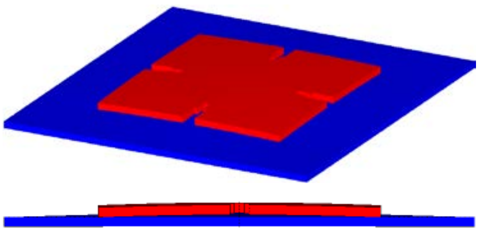		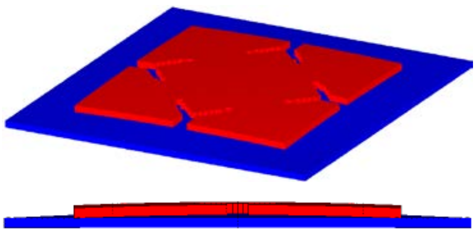	

Table.2 depicts similar microstructural topologies for the designed cells that possess the same curved angle θ but different side length ratio q, whereas, the obtained topologies are quite different for those under the same q and different θ. From the results given in Table.2(a) and (b), the stiffness represented by the k_{ss} decreases with the increase of q when desired in-plane ZTE is achieved. The stiffness decreasing is due to that, although more material volume fraction f_v is used, larger q implies the cells possessing larger design domain in the optimization process, resulting larger equivalent initial curvatures, which is the most important factor for in-plane stiffness loss. In the other aspect, as for the cases presented in Table.2(a), (c) and (e) with the same side length ratio q, the decreased initial curved angle θ reinforces the in-plane stiffness of the designed cells. However, the cost of this reinforcement is that more high CTE materials are required to achieve the in-plane ZTE. This finding also confirms the previous conclusion that the designs for ZTE with high stiffness usually lead to the increase of cell weight.

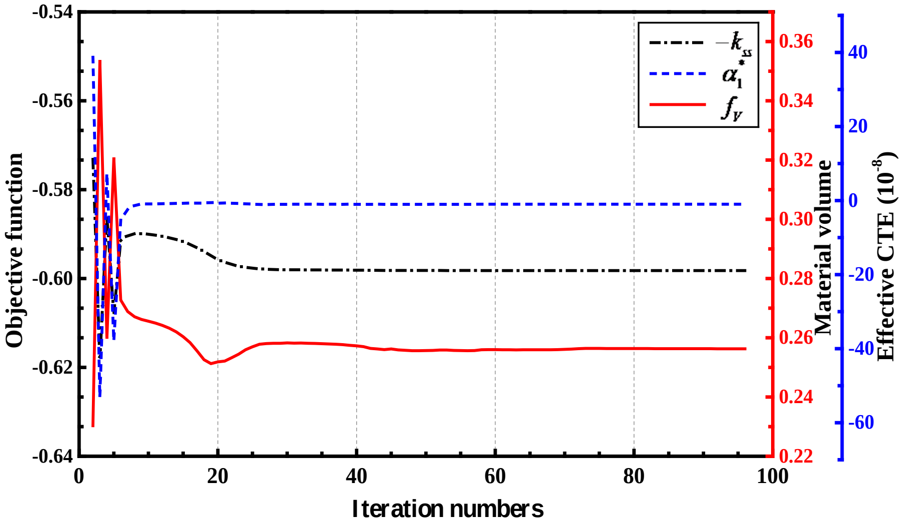

Fig.7. Iteration histories of the objective function $-k_{ss}$, high CTE material volume fraction f_V and effective CTE α_1^* of the design case with θ=4.5° and q=0.7.

Fig.7 shows the iteration histories of the objective function $-k_{ss}$, high CTE material volume fraction f_v and effective CTE α_1^* from the design case with θ=4.5° and q=0.7. The effective in-plane CTE eventually converges to the value of -1×10^{-8}, i.e., two-order decreasing of CTE compared with the constituent materials. The topology optimization process converges very fast within the first thirty steps. This illustration validates the effectiveness of the optimization algorithm proposed for the design of cell microstructures with specific thermal expansion and mechanical properties.

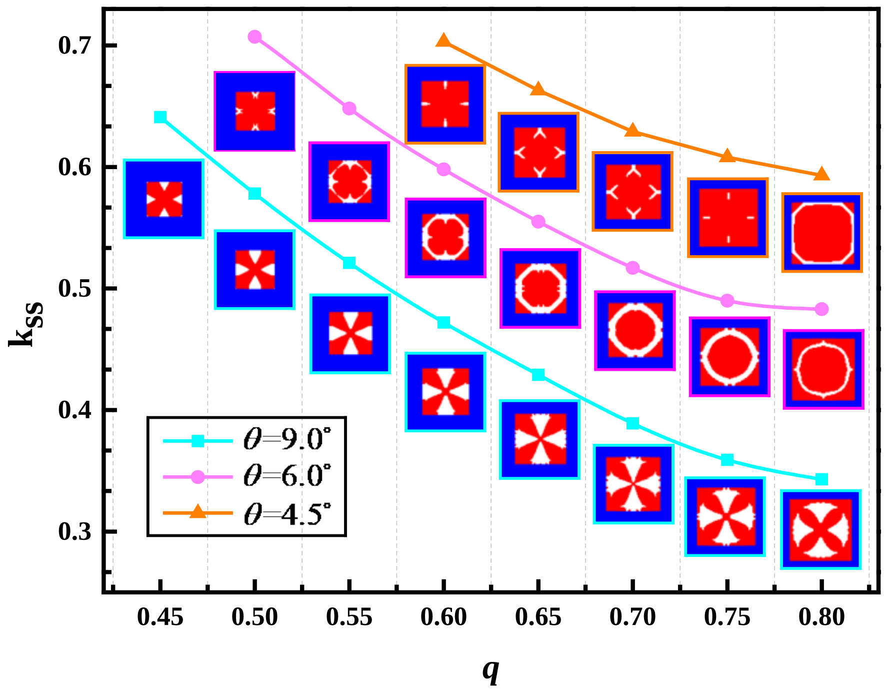

Fig.8. The feasible optimization solutions of cell microstructure for in-plane ZTE combining maximized stiffness with $\theta = 4.5°$, 6.0° and 9.0°.

For the curved angle of 4.5°, 6.0° and 9.0°, all of the feasible optimization solutions for the cell microstructures with maximum stiffness and in-plane ZTE are shown in Fig.8. The amount of feasible optimization solutions for small curved angles are less than those given by large angles, which is predetermined by considering the thermal bending-adjustment mechanism. As the constraint of desired in-plane ZTE is set in the optimization process, the cases with small curved angle require more materials with high CTE to trigger the thermally induced transverse bending, which restricts a great of design domain that can be used for optimization. Since the area of design domain represented by q is specific, thus the cases with small curved angle are likely leading to the failure of optimization process.

5.2 In-plane ZTE combining maximized specific stiffness

As aforementioned, the designs for in-plane ZTE with high stiffness usually lead to an increasing of cell weight. In this subsection, the topology optimizations for designing cell microstructures with both high stiffness and light weight as defined in Eq.(3) are carried out. Selected optimization results for the cell microstructures and the corresponding 3×3 arrays are shown in Table.3.

Table.3. Optimization solutions of cell microstructure and corresponding 3D view of the entire cell shapes and 3×3 arrays of the optimized cells under different curved angle θ and side length ratio q. The red and blue colors represent the materials with high and low CTE, respectively. The yellow border is the plane projection of designable layer which shows specific optimization design area.

θ (°)	$q = 0.6$		$q = 0.7$	
	Unit cell	Array (3×3)	Unit cell	Array (3×3)

9.0	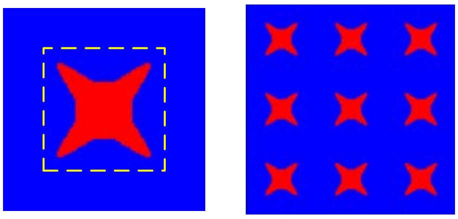	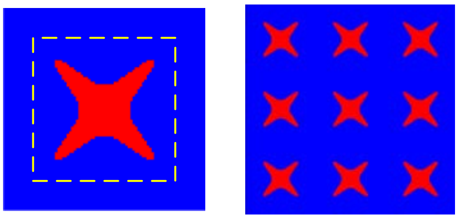
	(a) k_{sp} =3.866, f_V =0.120	(b) k_{sp} =3.159, f_V =0.120
3D view	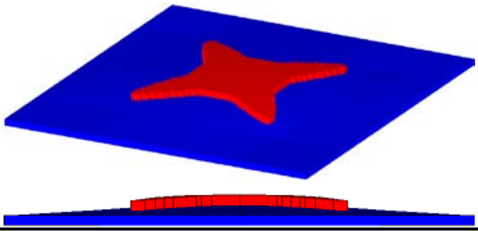	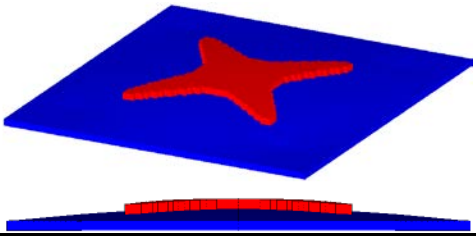
6.0	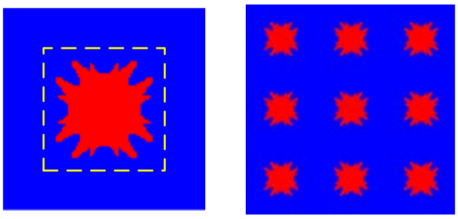	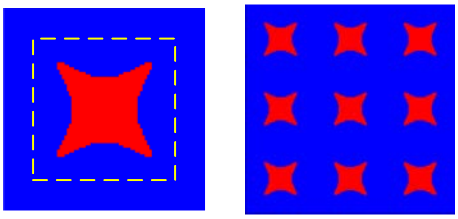
	(c) k_{sp} =3.910, f_V =0.151	(d) k_{sp} =3.562, f_V =0.141
3D view	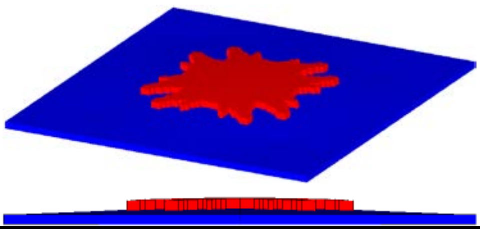	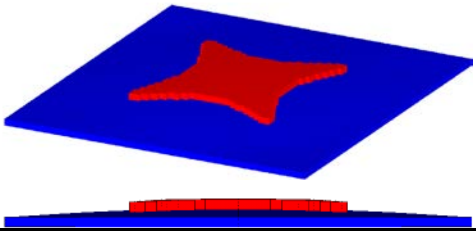
4.5	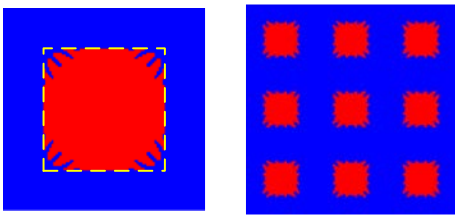	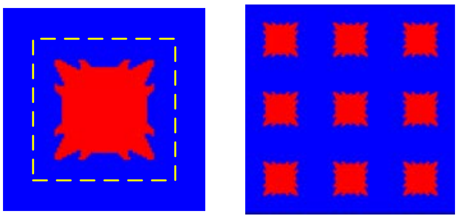
	(e) k_{sp} =3.230, f_V =0.215	(f) k_{sp} =3.152, f_V =0.194
3D view	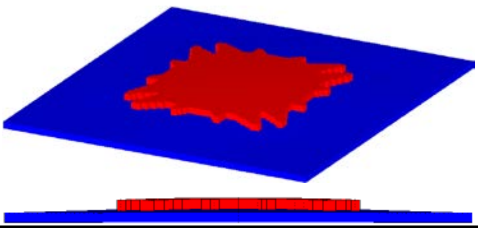	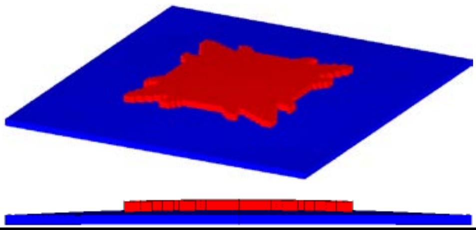

Table.3 depicts a distinct feature of cell microstructures that the distribution of high CTE material is mainly concentrated in both sides of the cell microstructural diagonal. This feature obtained from topology optimization possesses high effectiveness for controlling thermal deformation, which enables the least f_V required for obtaining near zero in-plane thermal expansion. As a result, the relative high stiffness, minimum weight, and the feature of in-plane

ZTE are achieved, simultaneously.

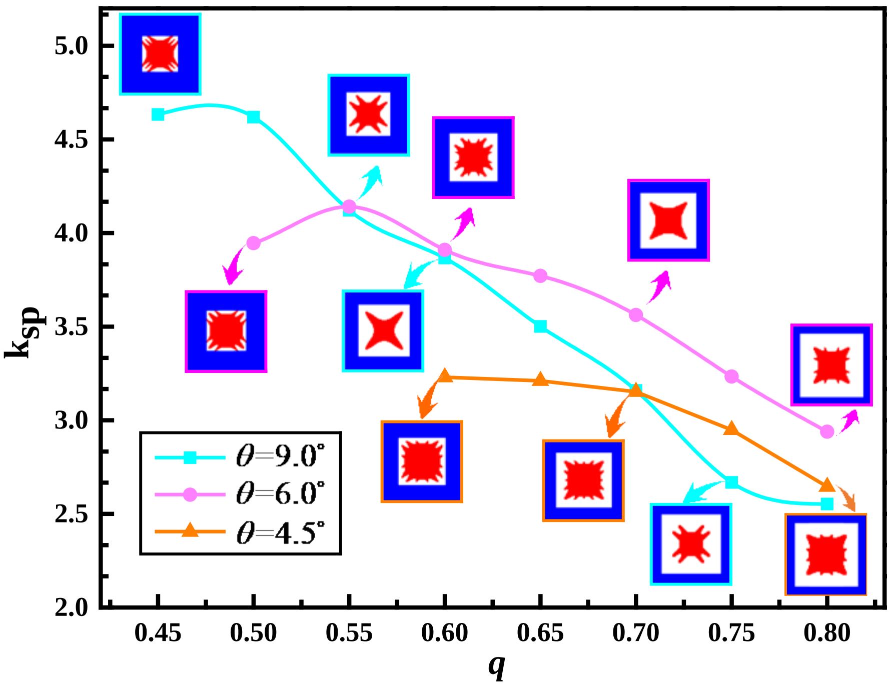

Fig.9. The feasible optimization solutions of cell microstructure for in-plane ZTE combining maximized specific stiffness with θ = 4.5°, 6.0° and 9.0°.

All of the feasible optimization results with curved angle of 4.5°, 6.0° and 9.0° for maximizing the specific stiffness with in-plane ZTE are shown in Fig.9. Some typical topologies are selected from all the design results for the purpose of illustration. As we adopt an appropriate initial curvature, the specific stiffness of optimized microstructures with small curved angles are weaker than those with large angles, such as θ=4.5° and 6.0°. This trend is contrary to the optimization results presented in Fig.8 for optimizing the maximum stiffness, only. For specific curved angles of θ=6.0° and 9.0°, decreasing of side length ratio q leads to the increase of optimized specific stiffness represented by k_{sp} firstly, and then the decreasing. Consequently, an optimization design domain needs to be found during the optimization process of microstructural topology for obtaining the maximum specific stiffness.

5.3 Minimized isotropic thermal expansion

The last optimization problem for obtaining the minimum in-plane thermal expansion without stiffness constraint is performed. The corresponding expression of objective function is given in Eq.(4), and the selected optimization results of cell microstructure and the corresponding 3×3 arrays are shown in Table.4.

Table.4. Optimization solutions of cell microstructure and corresponding 3D view of the entire cell shapes and 3×3 arrays of the optimized cells under different curved angle θ and side length ratio q.

θ (°)	$q = 0.6$		$q = 0.9$	
	Unit cell	Array (3 × 3)	Unit cell	Array (3 × 3)

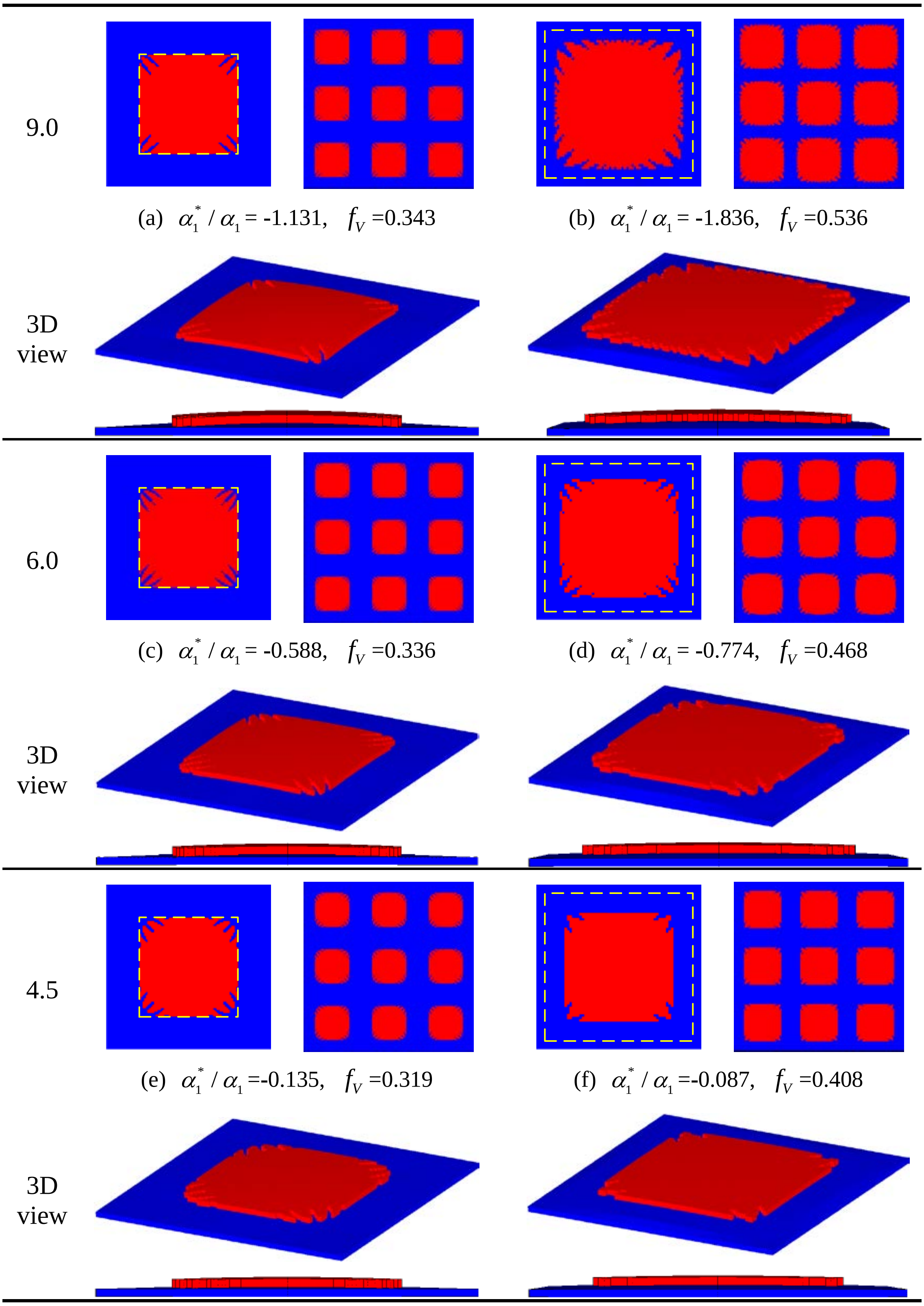

(a) $\alpha_1^* / \alpha_1 = -1.131$, $f_V = 0.343$

(b) $\alpha_1^* / \alpha_1 = -1.836$, $f_V = 0.536$

(c) $\alpha_1^* / \alpha_1 = -0.588$, $f_V = 0.336$

(d) $\alpha_1^* / \alpha_1 = -0.774$, $f_V = 0.468$

(e) $\alpha_1^* / \alpha_1 = -0.135$, $f_V = 0.319$

(f) $\alpha_1^* / \alpha_1 = -0.087$, $f_V = 0.408$

As we can see in Table.4, the microstructural topologies for minimum in-plane thermal expansion represented by the ratio of α_1^* / α_1 is obtained through optimizing the distribution of high CTE material with finite material volume. The completely covering patch layer like the original design configuration shown in Fig.3(a) brings excessive material with high CTE, which weakens the thermally induced transverse bending, and consequently leads to the increase of cell effective CTEs. Another distinct feature of cell microstructure obtained in the topology optimization is that the distribution of high CTE material is concentrated in the center of the design domain, in which the material distribution provides strong bending stiffness that induces the in-plane contraction to compensate the in-plane thermal expansion to a maximum extent.

The optimization results with curved angles of 4.5°, 6.0° and 9.0° are shown in Fig.10. Simultaneously, some typical topologies are chosen from all the optimal microstructures for the purpose of illustration. The effective in-plane CTEs of the optimal microstructures decrease with the increase of side length ratio q at first, and then increasing. Therefore, as for specific initial curvature, there will be an optimal design domain area for obtaining global optimal solution with minimum in-plane thermal expansion.

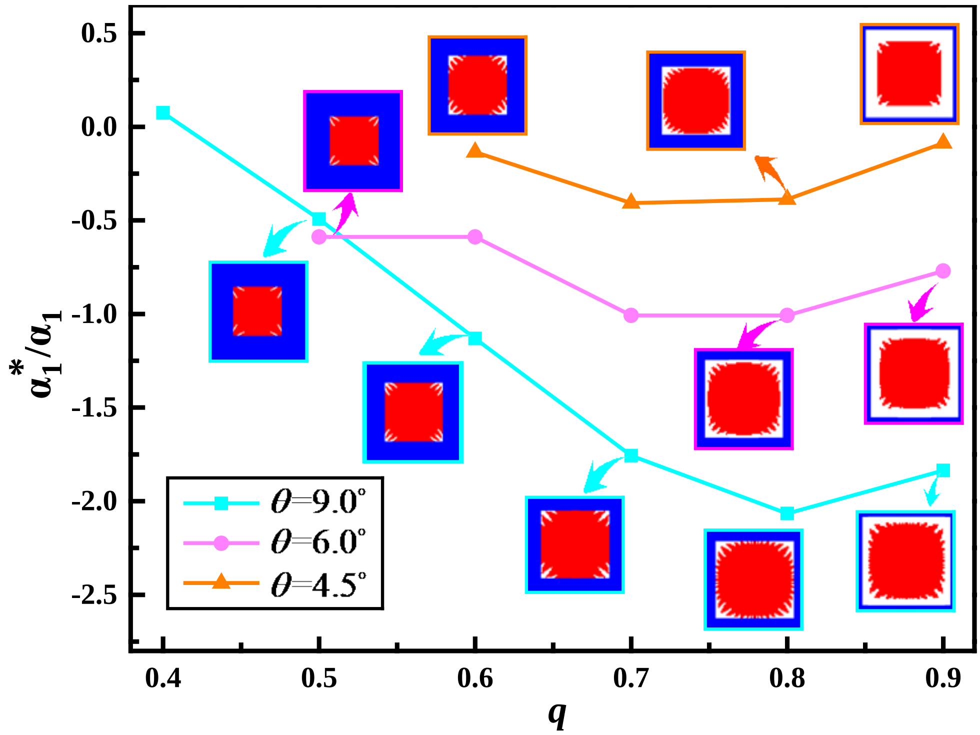

Fig.10. The feasible optimization solutions of cell microstructure for minimized isotropic thermal expansion with θ = 4.5°, 6.0° and 9.0°.

6. Conclusion

In this paper, we integrates the effective thermal adjustment mechanism and topology optimization technology to design the material microstructures for achieving specific in-plane CTEs with lightweight and/or benign mechanical properties. The in-plane thermal expansion tunability is ranging from negative to positive including zero. The whole topological process is performed within an in-house programme coupled with commercial finite element analysis software. Toward this end, we develop a matching numerical sensitivity analysis method to extract sensitivities straightforwardly from software's output. Three types of typical optimization problems considering the practical engineering demands are proposed, studied and solved.

Optimization results reveal that the microstructures with in-plane ZTE for higher stiffness usually lead to the increase of cell weight. For the design cases with in-plane ZTE and maximum specific stiffness, a distinct feature of cell microstructure is that the material distribution with high CTE is mainly concentrated at both sides of the diagonal of cell microstructure. The minimum in-plane isotropic CTEs are obtained by means of optimal material distribution with high CTE and specific finite volume, however, excessive use of material distribution is counterproductive. In summary, the major novelty of this work is developing an unified optimization strategy that integrates the existing functional mechanism and topology optimization techniques for the design of cell microstructure. In future work, this strategy will be extended to devise controllable CTEs metamaterials with robust mechanical properties by replacing present thermal deformation control mechanism.

Acknowledgements

The work is supported by National Nature Science Foundation of China (Grant no. 11972105, U1808215). We would also like to thank the Fundamental Research Funds for the Central Universities.

Compliance with ethical standards

Conflict of interest The authors declare that they have no conflict of interest.

Replication of results The results presented in this work are based on the flowchart shown in Fig.4. In order to replicate the results, a series of Matlab code is provided as supplementary material. The attached main program is named as “MATDesign_CTE.m” and other function programs are utilized to compute equivalent mechanical properties and the necessary sensitivity information in case 5.1. For replication of the results of other cases in the proposed work, the resulting designs can be obtained through modifying objective functions and constrain conditions to those in Eq.(7) and Eq.(8).

References:

Ai L, Gao XL (2019) Topology optimization of 2-D mechanical metamaterials using a parametric level set method combined with a meshfree algorithm Compos Struct 229:111318

Andreassen E, Lazarov BS, Sigmund O (2014) Design of manufacturable 3D extremal elastic microstructure Mech Mater 69:1-10 doi:https://doi.org/10.1016/j.mechmat.2013.09.018

Bendsoe MP, Kikuchi N (1988) Generating optimal topologies in structural design using a homogenization method

Bruns TE, Tortorelli DA (2001) Topology optimization of non-linear elastic structures and compliant mechanisms Computer Methods in Applied Mechanics & Engineering 190:3443-3459

Chen PC, Liu DD, Chang KT, Tang L, Wei S. (Aerothermodynamic Optimization of Hypersonic Vehicle TPS Design by POD/RSM-Based Approach44th AIAA Aerospace Sciences Meeting and Exhibit, 2006

Cheng GD, Cai YW, Xu L (2013) Novel implementation of homogenization method to predict effective properties of periodic materials Acta Mech Sinica-Prc:550-556

Kai W, Haosen C, Yongmao P, Daining F (2016) Planar lattices with tailorable coefficient of thermal expansion and high stiffness based on dual-material triangle unit J Mech Phys Solids 86:173-191

Lakes R (2007) Cellular solids with tunable positive or negative thermal expansion of unbounded magnitude Appl Phys Lett 90:359

Lehman J, Lakes R (2013) Stiff, strong zero thermal expansion lattices via the Poisson effect J Mater Res 28:2499-2508

Ni X, Guo X, Li J, Huang Y, Zhang Y, Rogers JA (2019) 2D Mechanical Metamaterials with Widely Tunable Unusual Modes of Thermal Expansion Adv Mater

Sigmund O (1995) Tailoring materials with prescribed elastic properties Mech Mater 20:351-368 doi:https://doi.org/10.1016/0167-6636(94)00069-7

Sigmund O, Torquato S (1997) Design of materials with extreme thermal expansion using a three-phase topology optimization method Journal of the Mechanics & Physics of Solids 45:1037-1067

Steeves CA, Evans AG (2011a) Optimization of Thermal Protection Systems Utilizing Sandwich Structures with Low Coefficient of Thermal Expansion Lattice Hot Faces J Am Ceram Soc 94:s55-s61

Steeves CA, Evans AG (2011b) Optimization of Thermal Protection Systems Utilizing Sandwich Structures with Low Coefficient of Thermal Expansion Lattice Hot Faces J Am Ceram Soc 94:s55-s61

Steeves CA, He M, Maxwell PT, Evans AG. (Design of a Robust, Multifunctional Thermal Protection System Incorporating Zero Expansion LatticesASME 2007 International Mechanical Engineering Congress and Exposition, 2007255-260

Steeves CA, Lucato SLDS, He M, Antinucci E, Hutchinson JW, Evans AG (2007) Concepts for structurally robust materials that combine low thermal expansion with high stiffness Journal of the Mechanics & Physics of Solids 55:1803-1822

Svanberg K (1987) The method of moving asymptotes—a new method for structural optimization Int J Numer Meth Eng 24:359-373 doi:10.1002/nme.1620240207

Takenaka, Koshi (2012) Negative thermal expansion materials: technological key for control of thermal expansion Ence & Technology of Advanced Materials 13:13001

Takezawa A, Kobashi M, Kitamura M (2015) Porous composite with negative thermal expansion obtained by photopolymer additive manufacturing Apl Mater 3:1477-1917

Torquato OSAS (1999) Design of smart composite materials using topology optimization Smart Mater Struct

Torquato SAS (1997) Design of materials with extreme thermal expansion using a three-phase topology optimization method

Wang B, Yan J, Cheng G (2011) Optimal structure design with low thermal directional expansion and high stiffness Eng Optimiz 43:581-595

Watts S, Tortorelli DA (2017) Optimality of thermal expansion bounds in three dimensions Extreme Mechanics Letters 12:97-100

Wei K, Peng Y, Wang K, Duan S, Yang X, Wen W (2018) Three dimensional lightweight lattice structures with large positive, zero and negative thermal expansion Compos Struct 188

Wu L, Li B, Zhou J (2016) Isotropic Negative Thermal Expansion Metamaterials Applied materials and Interfaces

Xia L, Breitkopf P (2015) Design of materials using topology optimization and energy-based homogenization approach in Matlab Vol.,

Xie Y, Lu D, Yu J. (Bimaterial Micro-Structured Annulus With Zero Thermal Expansion CoefficientAsme International Design & Engineering Technical Conferences & Computers &

Information in Engineering Conference, 2017

Xie Y, Pei X, Yu J (2018a) Double-layer sandwich annulus with ultra-low thermal expansion Compos Struct 203:709-717 doi:https://doi.org/10.1016/j.compstruct.2018.07.075

Xie Y, Pei X, Yu J (2018b) Double-layer sandwich annulus with ultra-low thermal expansion Compos Struct 203:709-717 doi:https://doi.org/10.1016/j.compstruct.2018.07.075

Xu H, Farag A, Pasini D (2017a) Multilevel hierarchy in bi-material lattices with high specific stiffness and unbounded thermal expansion Acta Mater 134:155-166 doi:https://doi.org/10.1016/j.actamat.2017.05.059

Xu H, Farag A, Pasini D (2017b) Multilevel hierarchy in bi-material lattices with high specific stiffness and unbounded thermal expansion Acta Mater 134:155-166 doi:https://doi.org/10.1016/j.actamat.2017.05.059

Xu H, Pasini D (2016) Structurally Efficient Three-dimensional Metamaterials with Controllable Thermal Expansion Sci Rep-Uk 6:34924

Yamamoto N, Gdoutos E, Toda R, White V, Manohara H, Daraio C Thin Films with Ultra‐low Thermal Expansion Adv Mater 26:3076-3080

Yi S, Cheng G, Xu L (2016) Stiffness design of heterogeneous periodic beam by topology optimization with integration of commercial software Comput Struct 172:71-80

Zhang H, Luo Y, Kang Z (2018) Bi-material microstructural design of chiral auxetic metamaterials using topology optimization Compos Struct:S342817304

Zhang Y, Liang Y, Liu S, Wang B (2018) A new design for enhanced stiffness of dual-constituent triangular lattice metamaterial with unbounded thermal expansion Mater Res Express 6

Zhang Y, Liang Y, Yang Z, Wang B, Liu S (2019) A new design concept of dual-constituent sandwich panel with in-plane zero thermal expansion Smart Mater Struct 28:65002 doi:10.1088/1361-665x/ab135b

Zhang Y, Shang S, Liu S (2017) A novel implementation algorithm of asymptotic homogenization for predicting the effective coefficient of thermal expansion of periodic composite materials Acta Mech Sinica-Prc 33:368-381

Zhang YC, Liang YJ, Liu ST, Su YD (2019) A new design of dual-constituent triangular lattice metamaterial with unbounded thermal expansion.

Zhengchun D, Mengrui Z, Zhiguo W, Jianguo Y Design and application of composite platform with extreme low thermal deformation for satellite Compos Struct:S344820395

Zhu H, Fan T, Peng Q, Zhang D (2018) Giant Thermal Expansion in 2D and 3D Cellular Materials. Adv Mater 30:e1705048

Appendix A: Implementation steps of NSAM-CTE

Similar with the implementation mode of NIAH-CTE for predicting the effective CTEs of periodic microstructures, the present NSAM-CTE can be implemented using the simulation capacity of commercial FEA soft as a black box. The sensitivity information in the form of element strain energy can be extracted directly from the output of FEA software, which substantially reduce the computational cost compared with that of using traditional methods. The concrete implementation steps of NIAH-CTE for predicting the sensitivities of the effective CTE $\partial \boldsymbol{\alpha}_i^{\boldsymbol{H}} / \partial \rho_e$ are given as follows:

Step 1: Build the finite element model for cell microstructure using standard modelling process;

Step 2: Predict the effective elastic modulus $\boldsymbol{E}^{\boldsymbol{H}}$ and thermos-elastic constant $\boldsymbol{\beta}^{\boldsymbol{H}}$ of cell microstructure using numerical results given by NIAH-CTE;

Step 3: Apply the generalized strain fields $\overline{\boldsymbol{\varepsilon}}^{\boldsymbol{i}+\alpha}$ to the finite element model for element strain energy $WB_e^{i+\alpha}$. Note that the element strain energy caused by the specific strain fields can be obtained through applying equivalent nodal displacement fields on each node due to the essence of the NIAH method. we can just construct the nodal displacement fields $\chi^{\boldsymbol{0(i)}}$ - $\chi^{*\boldsymbol{(i)}}$ - $\chi^{\boldsymbol{\zeta}}$ and thermal loads (-1℃) for $\overline{\boldsymbol{\varepsilon}}^{\boldsymbol{i}+\alpha}$, and as input to the finite element model, the element strain energy $WB_e^{i+\alpha}$ can be extracted directly from the output of FEA software after one static analysis. The extractions for the element strain energies W_e^{ii} and WB_e^{α} are subsequently performed using the same implementation procedure;

Step 4: Calculate the sensitivities of the effective thermos-elastic constant $\partial \boldsymbol{\beta}^{\boldsymbol{H}} / \partial \rho_e$ from Eq.(17) - (23);

Step 5: Extract the sensitivities of the effective elastic modulus $\partial \boldsymbol{E}_{ij}^{\boldsymbol{H}} / \partial \rho_e$ from the output of FEA software using original numerical sensitivity analysis method (Yi et al. 2016). For the purpose of the brevity, the concrete implementation steps for obtaining $\partial \boldsymbol{E}_{ij}^{\boldsymbol{H}} / \partial \rho_e$ are not presented herein;

Step 6: Calculate the sensitivities of the effective CTE $\partial \boldsymbol{\alpha}_i^{\boldsymbol{H}} / \partial \rho_e$ from Eq.(16).

Appendix B: Method verification of NSAM-CTE

In order to verify the effectiveness of present NSAM-CTE for computing the sensitivities, a simple verification example is performed through comparing the sensitivity results with that obtained by the finite difference method (FDM). After establishing the finite element model of original design configuration as shown in Fig.3(a), three arbitrary elements are taken as the testing cases for verifications. The comparison results of $\partial \boldsymbol{E}_{ij}^{\boldsymbol{H}} / \partial \rho_e$ and $\partial \boldsymbol{\alpha}_i^{\boldsymbol{H}} / \partial \rho_e$ given by NSAM-CTE and FDM are listed in Table.5 and Table.6, respectively. The finite-difference interval $\Delta\rho$ for FDM is taken as 1×10^{-4}.

Table.5. The sensitivity comparison results of $\partial \boldsymbol{E}_{ij}^{\boldsymbol{H}} / \partial \rho_e$.

$\partial \boldsymbol{E}_{ij}^{\boldsymbol{H}} / \partial \rho_e$	Test element 1		Test element 2		Test element 3	
	NSAM	FDM	NSAM	FDM	NSAM	FDM
$\boldsymbol{E}_{11}^{\boldsymbol{H}}$	16300	16300	293760	293660	137740	137740
$\boldsymbol{E}_{22}^{\boldsymbol{H}}$	137640	137640	293520	293650	16380	16380
$\boldsymbol{E}_{33}^{\boldsymbol{H}}$	47330	47320	54020	54020	47500	47480
$\boldsymbol{E}_{12}^{\boldsymbol{H}}$	-3070	-3070	-150360	-150370	-3170	-3170

Table.6. The sensitivity comparison results of $\partial \boldsymbol{\alpha}_i^{\boldsymbol{H}} / \partial \rho_e$.

$\partial \boldsymbol{\alpha}_{ij}^{\boldsymbol{H}} / \partial \rho_e$	Test element 1		Test element 2		Test element 3	
	NSAM	FDM	NSAM	FDM	NSAM	FDM
$\boldsymbol{\alpha}_{11}^{\boldsymbol{H}}$	0.2086	0.2086	-0.2682	-0.2681	-0.2613	-0.2613
$\boldsymbol{\alpha}_{22}^{\boldsymbol{H}}$	-0.2615	-0.2615	-0.2685	-0.2684	0.2098	0.2098

It can be seen from Table.5 and Table.6 that the sensitivity results of main in-plane coefficients of effective elastic modulus and CTEs match very well with the results computed using FDM. As such the effectiveness of the present numerical sensitivity analysis method and corresponding implementation steps are verified.